JAMES | Journal of Advances in Modeling Earth Systems

RESEARCH ARTICLE
10.1029/2022MS003534

Statistics of the Subgrid Cloud of an Idealized Tropical Cyclone at Convection-Permitting Resolution

Xu Zhang[1,2], Jian-Wen Bao[3], Wei Huang[1,2], and Hui Yu[1,2]

[1]Shanghai Typhoon Institute, China Meteorological Administration, Shanghai, China, [2]Key Laboratory of Numerical Modeling for Tropical Cyclone, China Meteorological Administration, Shanghai, China, [3]NOAA/Earth System Research Laboratory, Boulder, CO, USA

Key Points:

- Tropical cyclone (TC) large-eddy simulations were conducted as benchmarks to provide statistical information about subgrid cloud at convection-permitting resolution
- Subgrid convective clouds were mainly located in the lower troposphere, and exhibited shallow vertical extents of less than 4 km
- Local subgrid clouds differed in mass-flux profile shape and magnitude at various cloud regimes in the TC convection system

Supporting Information:

Supporting Information may be found in the online version of this article.

Correspondence to:

X. Zhang,
zhangx@typhoon.org.cn

Citation:

Zhang, X., Bao, J.-W., Huang, W., & Yu, H. (2023). Statistics of the subgrid cloud of an idealized tropical cyclone at convection-permitting resolution. *Journal of Advances in Modeling Earth Systems*, *15*, e2022MS003534. https://doi.org/10.1029/2022MS003534

Received 22 NOV 2022
Accepted 18 MAY 2023

Author Contributions:

Conceptualization: Jian-Wen Bao
Data curation: Xu Zhang
Formal analysis: Xu Zhang
Funding acquisition: Xu Zhang, Wei Huang, Hui Yu
Investigation: Xu Zhang, Jian-Wen Bao
Methodology: Xu Zhang
Project Administration: Xu Zhang, Wei Huang, Hui Yu

Abstract Large-eddy simulations of an idealized tropical cyclone (TC) were conducted as benchmarks to provide statistical information about subgrid convective clouds at a typical convection-permitting resolution of 3 km over a TC convection system in different stages. The focus was on the vertical and spatial distributions of the subgrid cloud and associated mass flux that need to be parameterized in convection-permitting models. Results showed that the characteristics of the subgrid clouds varied significantly in various parts of the TC convection system. Statistical analysis revealed that the subgrid clouds were mainly located in the lower troposphere and exhibited shallow vertical extents of less than 4 km. The subgrid clouds were also classified into various cloud regimes according to the maximum mass flux height. Local subgrid clouds differed in mass-flux profile shape and magnitude at various regimes in the TC convection system.

Plain Language Summary High-resolution large-eddy simulations of an idealized tropical cyclone (TC) were conducted as baselines to provide a statistical picture of subgrid clouds in an idealized TC simulation at 3 km resolution. Most of the subgrid clouds showed shallow vertical thicknesses of less than 4 km and were located in the lower troposphere, which are different from the average properties of the clouds over the entire model domain. The characteristics of subgrid clouds showed a large spatial variability of cloud top height, cloud depth and updraft mass flux within the simulation domain. This demonstrated limitations of applying most conventional convection parameterizations, which do not take account of the spatial variability of subgrid clouds, to convection-permitting resolutions.

1. Introduction

The clouds in a tropical cyclone (TC) exhibit a large variety of processes and forms due to the underlying vortex dynamics. For physically realistic numerical simulations of TCs, the cloud processes must be adequately resolved or parameterized. Current operational numerical weather prediction (NWP) models for TC simulation and forecasting have a horizontal grid size on the order of 1 km, which is convection-permitting but not sufficient to resolve individual convective cells fully (e.g., Bryan et al., 2003; Moeng et al., 2010). Including subgrid parameterization of convection in the physics configuration is a practical means to account for the effect of unresolved convection on the resolved TC dynamics.

For practical uses in NWP models, scale-adaptive algorithms of convective mass flux have been introduced into traditional quasi-equilibrium convection parameterization schemes that can be used at convection-permitting resolutions (Arakawa et al., 2011; Grell & Freitas, 2014; Han et al., 2017; Kwon & Hong, 2017). In such practices, the mass flux of deep convection is downscaled by a resolution-dependent scale factor to be adaptive at convection-permitting resolutions. At such resolutions, however, the traditional ensemble mean closure used to describe the collective effect of many individual subgrid clouds is inappropriate for representing subgrid-scale processes (Moeng et al., 2010). The subgrid-scale mass flux associated with convective clouds varies significantly in various parts of the convection system. The traditional parameterizations are expected to determine the ensemble mean effect of a wide range of subgrid convective states. What convection-permitting models need to parameterize are the local subgrid-scale mass flux within each grid box.

About half a century ago, the bulk properties of convective cloud ensemble were estimated from diagnostic analyses of radiosonde arrays (Yanai et al., 1973). Recently, Savazzi et al. (2021) estimated convective mass fluxes on the scale of a 100 km grid box from radar reflectivities spanning 13 wet seasons. These observational studies established reliable benchmarks for tropical cloud ensembles that needed to be parameterized in traditional

Resources: Xu Zhang
Software: Xu Zhang
Supervision: Wei Huang, Hui Yu
Validation: Xu Zhang
Visualization: Xu Zhang
Writing – original draft: Xu Zhang
Writing – review & editing: Xu Zhang, Jian-Wen Bao

cumulus convection parameterizations. However, at convection-permitting resolutions, miscellaneous practices of scale-adaptivity (Arakawa et al., 2011; Bechtold et al., 2008; Grell & Freitas, 2014; Han et al., 2017; Kwon & Hong, 2017; Zheng et al., 2016) point to the lacks of benchmark and consensus on the characteristics of subgrid cloud.

More recently, large-eddy simulation (LES) has become computationally feasible and offers an opportunity to study detailed information on subgrid cloud processes that cannot be observed. Khairoutdinov et al. (2009) conducted a LES of deep tropical convection in near equilibrium to investigate the vertical distribution and statistics of the cloud and suggested that the LES can be used as a benchmark to describe the dynamics of tropical deep convection on scales ranging from turbulence to mesoscale convective systems. Moeng and Arakawa (2012) used such LES data to test parameterizations for representing the spatial distribution of boundary layer moisture transport at convection-permitting resolution. Shi et al. (2019) performed a similar LES of an idealized case for deep tropical convection to evaluate the performance of turbulence models at convection-permitting resolution. The above-mentioned studies focused on the tropical convection systema at radiative-convective equilibrium. Due to the limitations of observations in time and space, the LES technique is also used to understand the small-scale coherent structures and associated roles in the evolution of TCs (Green & Zhang, 2015; Rotunno et al., 2009; Wu et al., 2018; Zhu, 2008; Zhu et al., 2019). Increasing observational evidence (Lorsolo et al., 2008; Marks et al., 2008; Morrison et al., 2005; Wurman & Kosiba, 2018; Wurman & Winslow, 1998) testifies the ability of LESs to realistically reproduce turbulent flow features in TCs.

In a TC system, the characteristics of convection in a diverse range of regions vary significantly due to the underlying dynamics (Houze, 2010). In addition to the radiative-convective equilibrium case, a TC system might be a more opportune convective case to investigate the properties of various clouds and their interaction with dynamical forcing. We still do not have a clear picture regarding the characteristics of subgrid cloud in TC convection systems and the associated subgrid-scale mass flux at convection-permitting resolution.

In this study, idealized TC LESs with 250 m horizontal grid size were conducted as benchmarks to investigate the characteristics of subgrid cloud at convection-permitting resolution. The 250 m horizontal grid size was a compromise between the domain size and the availability of computational resources. The objective of this paper is to provide statistical information about the subgrid clouds at convection-permitting resolution over a large TC system in different stages. Attention will be focused on the vertical and spatial distributions of subgrid clouds that occur within the grid boxes of convection-permitting models. The results of this study will provide suggestions and implications for the parameterization of subgrid cloud in convection-permitting models.

The paper is organized as follows: Section 2 describes the setup of the benchmark LES of an idealized TC in different development stages. The coarse-graining method and the definition and selection of statistical samples are explained in Section 3. Section 4 presents the statistical results of the characteristics of subgrid cloud within a 3 km × 3 km grid box and the composite analysis by maximum mass flux height. The results are summarized and the implications for parameterization are discussed in Section 5.

2. Benchmark: Large-Eddy Simulations of a Tropical Cyclone

Three-dimensional idealized simulations of a TC were performed using version 4.3.1 of the Advanced Research Weather Research and Forecasting Model (WRF) (WRF-ARW; Skamarock et al., 2019). We first conducted a TC simulation with a 3 km horizontal grid size. The initial axisymmetric vortex had a maximum lowest-level wind of 15 m s^{-1}, radius of maximum wind of 60 km, and radius of zero wind of 250 km. A smaller initial vortex than that of Rotunno and Emanuel (1987) was set to reduce the computational cost. The Coriolis parameter was set to be constant with its value at 20° latitude (5×10^{-5} s^{-1}). The initial conditions for potential temperature and humidity were obtained from the Jordan sounding (Jordan, 1958), as also used by Rotunno et al. (2009). The atmospheric radiation was represented by a capped Newtonian relaxation scheme, which is a crude approximation for longwave radiation. Air-sea exchange of heat and momentum was represented by a bulk aerodynamic formulation (Donelan et al., 2004). All simulation cases were run with a constant sea surface temperature of 28°C. Other physics options in the 3 km run included the Thompson microphysics scheme (Thompson et al., 2008) and the Yonsei University (YSU; Hong et al., 2006) planetary boundary layer parameterization. No cumulus convection scheme was used. The model domain was 600 km × 600 km in the horizontal plane with a vertical extension of 25 km (81 vertical levels). The lateral boundary conditions were double periodic. Time integration was performed for a 6-days period.

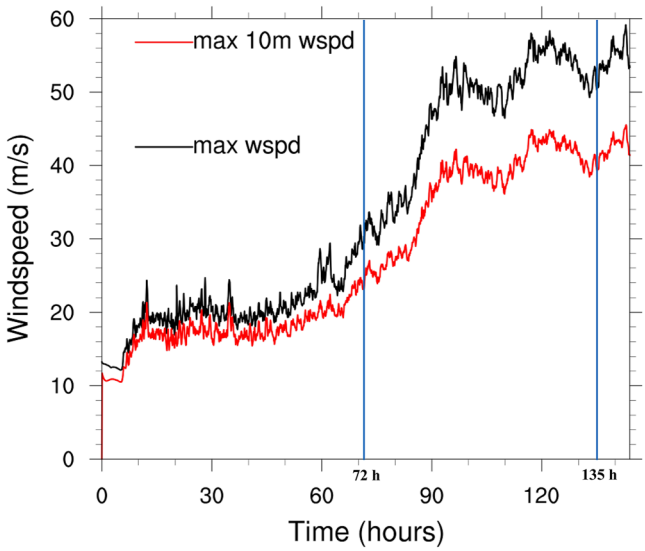

Figure 1. Time series of the instantaneous maximum horizontal wind speed (wspd, black) and maximum horizontal wind speed at the 10 m level (red) for the 3 km run. The vertical blue lines indicate the initialization times of the large-eddy simulation benchmarks.

Figure 1 shows the time series of the instantaneous maximum horizontal wind speed and maximum horizontal wind speed at the 10 m level for the 3 km run. The TC developed over about 96 hr before reaching a mature, statistically steady state. To investigate the characteristics of subgrid cloud in different TC development stages, two sets of benchmark LESs were performed with initializing at 72 and 135 hr, representing the stages of rapid intensification (RI) and maturity, respectively (Figure 1).

The horizontal grid size of the TC LES benchmark was 250 m. The LES benchmarks were initialized from interpolated 3 km fields at 250 m resolution when the TC was intensifying (72 hr) and fully developed (135 hr). The configuration of the LES benchmarks was the same as the 3 km run, except for the horizontal resolution. The 1.5-order 3D prognostic turbulent kinetic energy scheme (Deardorff, 1980) for subgrid mixing was used instead of the YSU scheme and 2D Smagorinsky closure (Smagorinsky, 1963). Unlike previous studies (e.g., Green & Zhang, 2015; Rotunno et al., 2009; Wu et al., 2018), which used the nested domain technique to conduct TC LESs, we did not use the nested technique because we wanted to avoid uncertainties from the parent domain. The domain sizes for the 3 km run and LES were kept the same as that of the LES, which had 2,400 × 2,400 mesh grids. The LES benchmarks were run for 3 hr (72–75 hr for the RI stage, 135–138 hr for the mature stage), and outputs were saved every 5 min. The analysis data was sampled every 5 min for the last 15 min of the 3 hr simulation, when the small-scale structures of cloud had fully developed.

The maximum wind speed from the LES reached nearly 80 m s^{-1} during t = 137–138 hr (Figure 2a). The LES instantaneous wind speed presented spatial patterns with randomly distributed, small-scale pockets of extreme wind speeds (Figure 2b), which were similar to previous LES experiments (Green & Zhang, 2015; Ren et al., 2020; Rotunno et al., 2009; Zhu et al., 2019). Ren et al. (2020) suggested that the grid size of 200 m is sufficient for a converged solution of the wind's statistical characteristics and the turbulent structures. Although the grid size of 250 m is relatively coarser than traditional LES grid sizes (<100 m), the above results suggested that the LES provided a suitable data set for investigating the cloud structure of the TC and the induced subgrid mass flux.

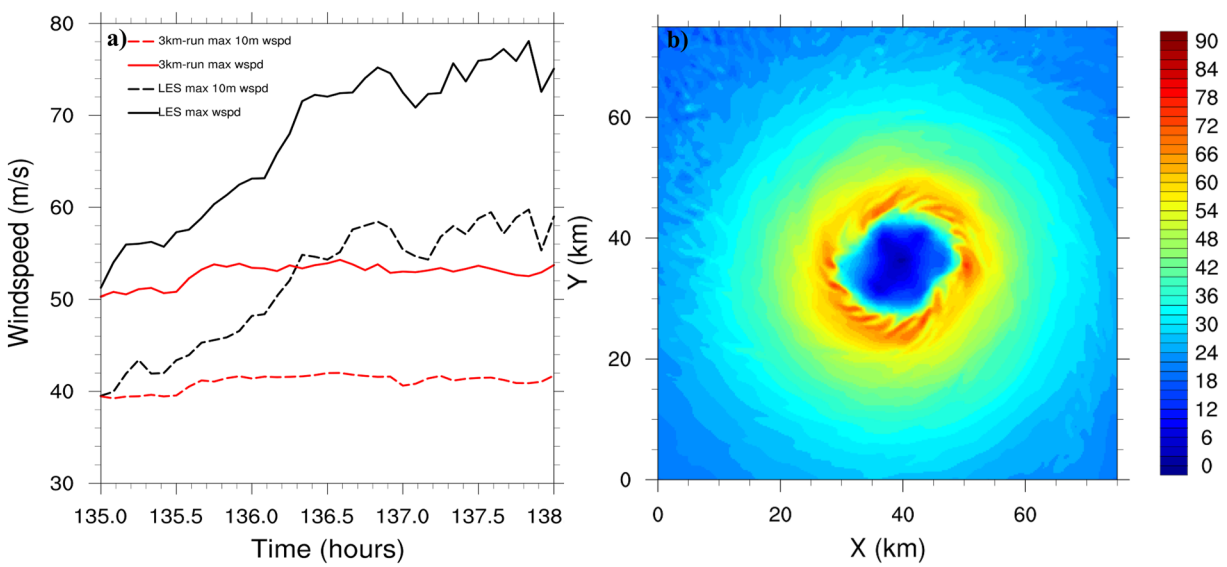

Figure 2. (a) Time series of the instantaneous maximum wind speed (wspd, solid lines) and maximum wind speed at the 10 m level (dashed lines) for the 3 km run (red lines) and large-eddy simulation (LES) (black lines) during the mature stage (135–138 hr); (b) Distribution of wind speed (unit: m s^{-1}) from the LES at the 500 m level at t = 138 hr.

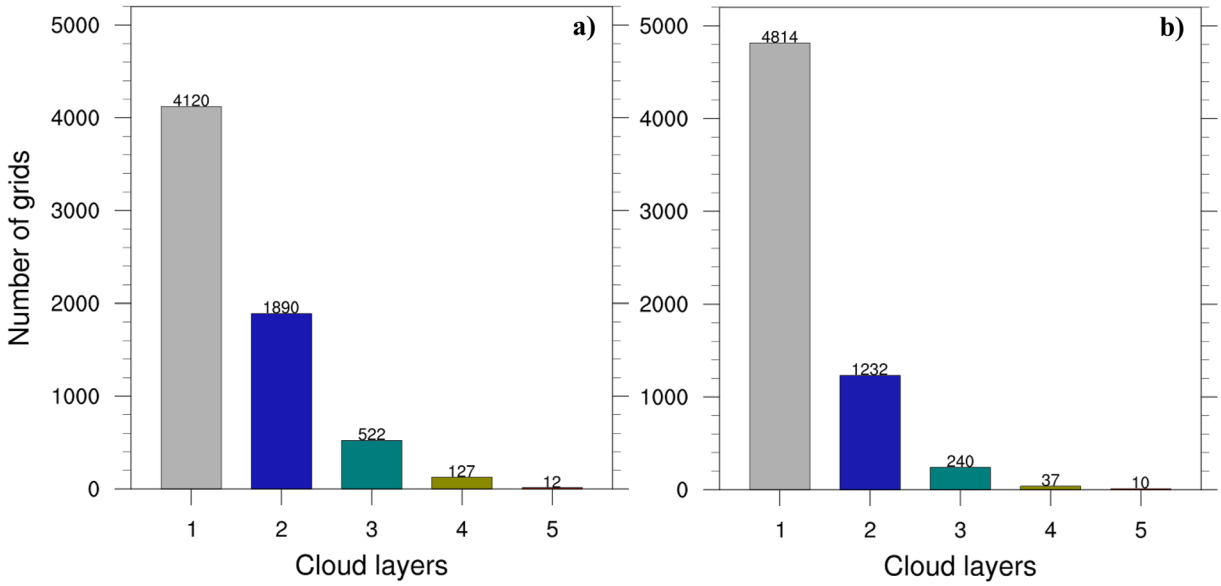

Figure 3. Histograms of grid columns with different cloud layers in the (a) rapid intensification and (b) mature stage.

3. Methodology

The LES model domain was divided into subdomains with a 3 km box size (a typical convection-permitting resolution). The benchmark LES fields were coarse-grained to obtain the subgrid convective characteristics at 3 km resolution (Honnert et al., 2011; Zhang et al., 2018). The LES coarse-grained updraft mass flux can be calculated by $M_u = \rho a_u (w_u - \overline{w})$, where a_u is the fractional area of the cloudy updraft, w_u is the vertical velocity of the cloudy updraft, $\overline{w}$ is the averaged vertical velocity over the 3 km × 3 km subdomain, and ρ the density. The mass flux refers to as the mass flux term used in convection schemes, which is obtained by neglecting the turbulence terms associated with the inhomogeneous properties within clouds and environment (Siebesma & Cuijpers, 1995). The cloudy updraft was defined as the LES grid points that contained cloud water and ice ($q_c + q_i > 1$ g/kg, with q_c and q_i denoting the cloud water and ice mixing ratio, respectively) and that had a positive vertical velocity ($w > 0$). At each vertical level and time, if the coarse-grained subdomain encompassed two or more cloudy LES grid points, the subdomain was defined as cloudy.

Because a key aim of this study was to study the vertical profiles of convective mass flux, only 3 km grid columns where the area fraction a_u at any level was greater than 0.01 (at least two cloudy LES grid points) were chosen as a statistical sample. The 3 km convective columns were then defined as the vertical region that contained at least one cloud layer. A cloud layer was a consecutive layer with mass flux greater than zero. The vertical column could contain more than one cloud layer, which were separated by the level with $M_u = 0$. The total number of samples of convective 3 km grid columns for the RI and mature stages was 6,673 and 6,333, respectively. Figure 3 shows histograms of the convective 3 km grid columns with different cloud layers in the RI and mature stages. Convective grid columns with single and two cloud layers constituted 90% of all samples. In this study, the cloud top height (CTH) in each 3 km grid column was defined as the height where $M_u = 0$ at the top of a column of consecutive mass flux greater than zero was reached. Note that "cloud" in this paper refers to subgrid cloud, which is an object that needs to be parameterized.

4. Results

Based on the above datasets and methods, a large number of samples of convective 3 km grid columns in the TC RI and mature stages were obtained. Statistical characteristics of the subgrid clouds at convection-permitting resolution are presented as follows.

4.1. Cloud Depth

The cloud depth was defined as the depth of a consecutive layer with subgrid mass flux greater than zero. About 62% (76%) of all convective columns contained a single cloud layer in the RI (mature) stage (Figures 3a and 3b).

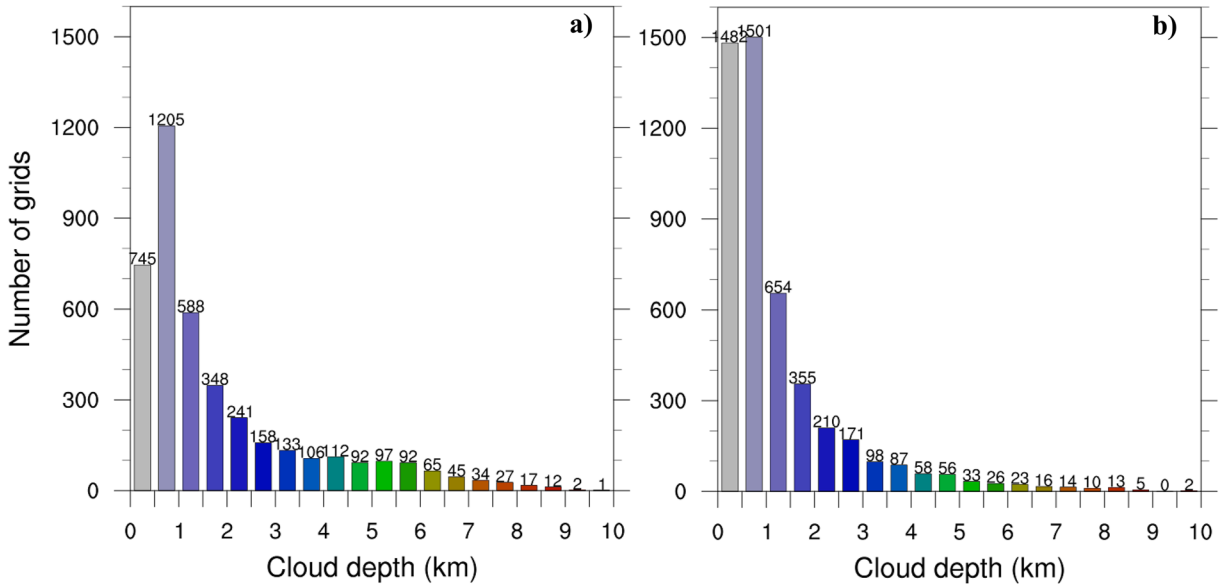

Figure 4. Histograms of cloud depth in convective columns with single-layer cloud in the (a) rapid intensification and (b) mature stage.

Figure 4 shows the distributions of cloud depth in convective columns with a single cloud layer in the RI and mature stages. Most cloud layers had a shallow vertical extent of less than 4 km. Compared to the RI stage (Figure 4a), more subgrid clouds tended to have a shallower vertical extent in the TC mature stage (Figure 4b).

Approximately 28% (19%) of all convective columns contained two cloud layers in the TC RI (mature) stage (Figures 3a and 3b). Figure 5 shows the distributions of cloud depth in convective columns with two cloud layers in the RI and mature stages. The top (bottom) panels present the cloud depth distributions of the lower (left) and upper (right) cloud layer in the RI (mature) stage. Like the single-layer case, the lower and upper layers of most two-layer clouds both had thicknesses of less than 4 km. In short, the vertical structures of subgrid clouds at convection-permitting resolution showed thin vertical extensions, implying that subgrid clouds can not only launch from surface, but also from any height.

4.2. Cloud Top Height

Figure 6 shows the CTH distributions for all convective columns in the RI and mature stages. In the RI stage (Figure 6a), there were two peaks representing two types of subgrid cloud with their CTH at about 2 and 5 km, respectively. As shown above, the cloud layers had shallow vertical extents. It can be inferred that the dominant mode of subgrid cloud shows that single or two cloud layers with thin thicknesses (<4 km) are most frequently seen at the height of 2 and/or 5 km. Compared to the RI stage, the mature phase presented more clouds with CTH below 2 km and fewer clouds with CTH at about 5 km (Figure 6b), which indicates the merger and axisymmetrization of convective towers during the mature stage (Bao et al., 2012; Montgomery & Smith, 2014; Nguyen et al., 2008). More buoyant convective towers were present during the RI stage, which was consistent with the results of numerical and observational studies (Bell & Montgomery, 2010; Houze et al., 2009; Nguyen et al., 2008).

Note that Figure 6 shows the CTH distributions of subgrid cloud rather than the resolved cloud; and subgrid cloud and resolved cloud do not necessarily have a corresponding relationship. In this study the subgrid cloud is defined by non-zero subgrid mass flux.

4.3. Updraft Mass Flux and Its Components

To gain more insight into the characteristics of subgrid cloud and to guide the parameterization, the statistics of the updraft mass flux in all convective columns are provided. Figure 7 shows the distributions of updraft mass flux M_u, area fraction a_u and net vertical velocity $w_u - \overline{w}$ for the RI and mature stages. All percentiles were calculated

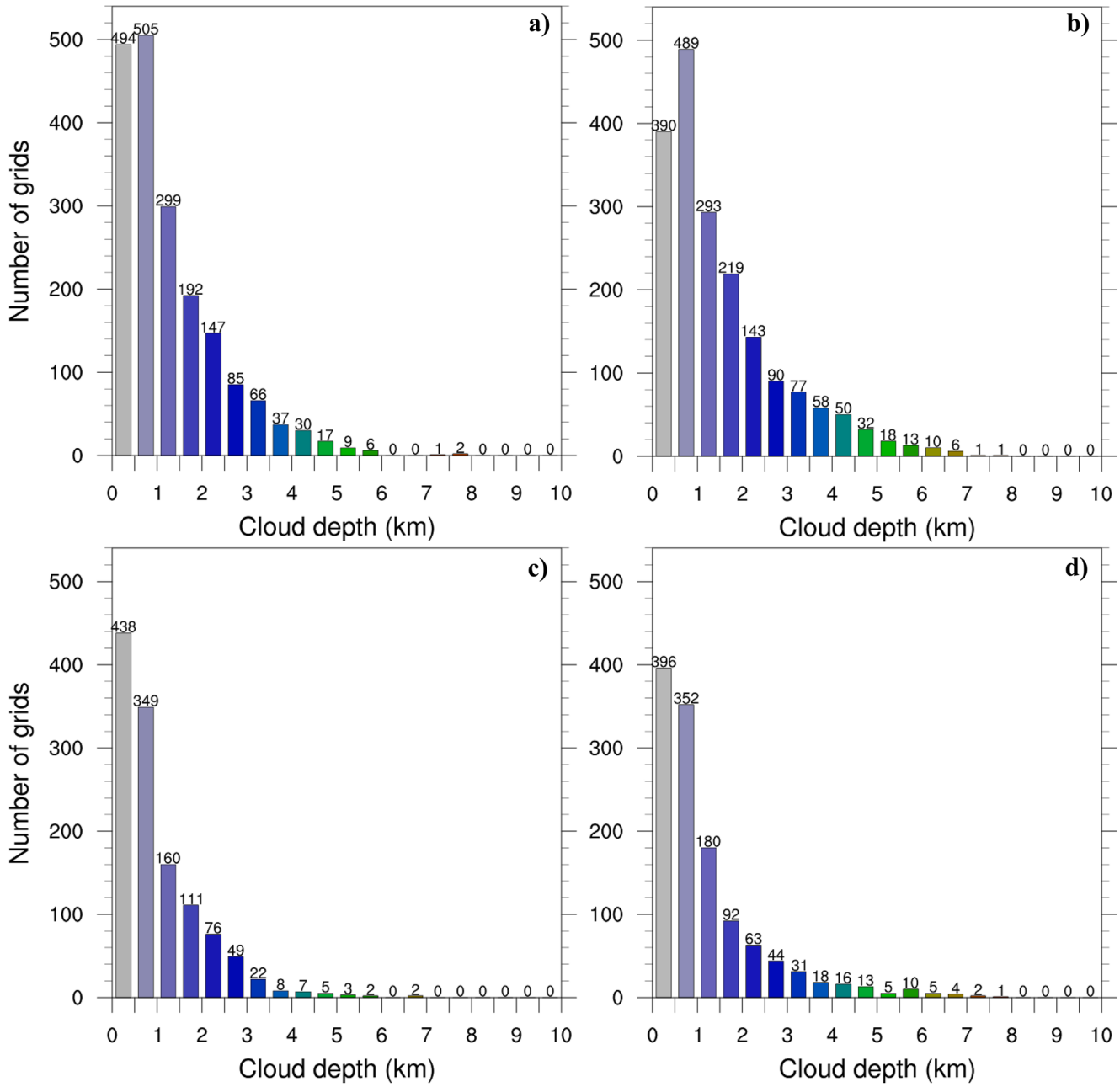

Figure 5. Histograms of cloud depth of the (a and c) lower and (b and d) upper layer in convective columns with two cloud layers in the (a and b) rapid intensification and (c and d) mature stage.

separately for each vertical level. The profiles of ensemble-mean mass flux (blue line in Figures 7a and 7d) show a well-known shape, with an increase in magnitude below 2 km and a gradual decrease with height (Böing et al., 2012). The profiles of the cloud ensemble indicate that fewer and fewer clouds reach the upper levels of the atmosphere. The traditional convection schemes based on ensemble-mean closure are expected to parameterize the ensemble mean profile of mass flux, but the ensemble mean is not needed in convection-permitting models.

The distribution shows significant skewness at all levels, with the upper quartile values being comparable to the mean. The large skewness of the distribution suggests that few local grid columns with strong mass flux shifted the distribution toward larger values. The convective area fraction was almost constant between 1.5 and 5 km (Figure 7b). The shape of the mean mass flux profile was largely determined by the decrease in net vertical velocity with height (Figure 7c).

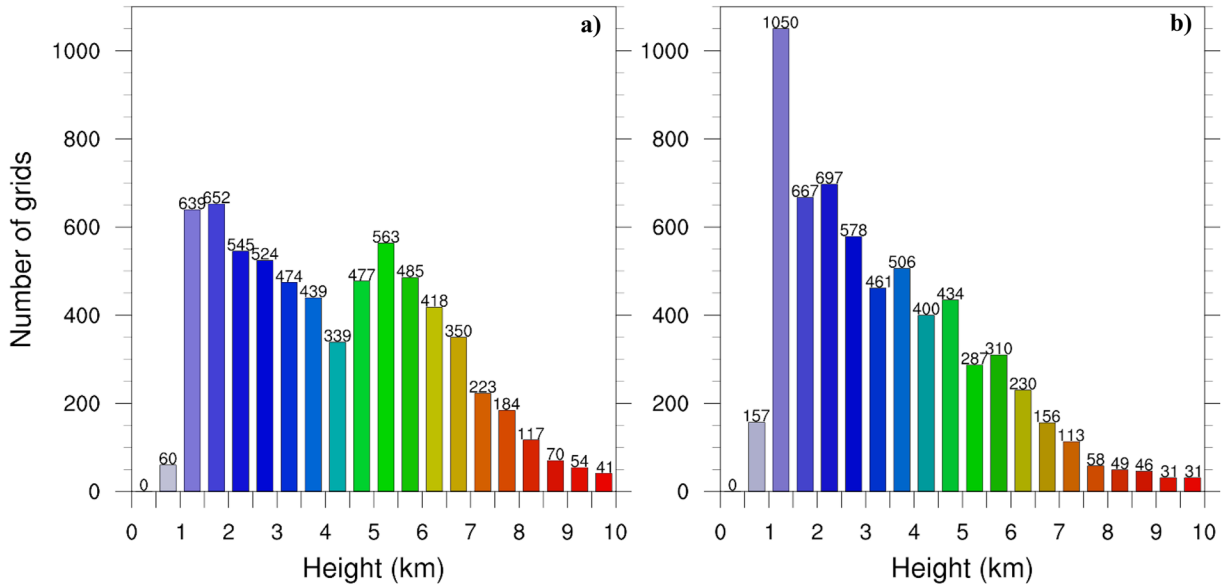

Figure 6. Histograms of cloud top height in the (a) rapid intensification and (b) mature stage.

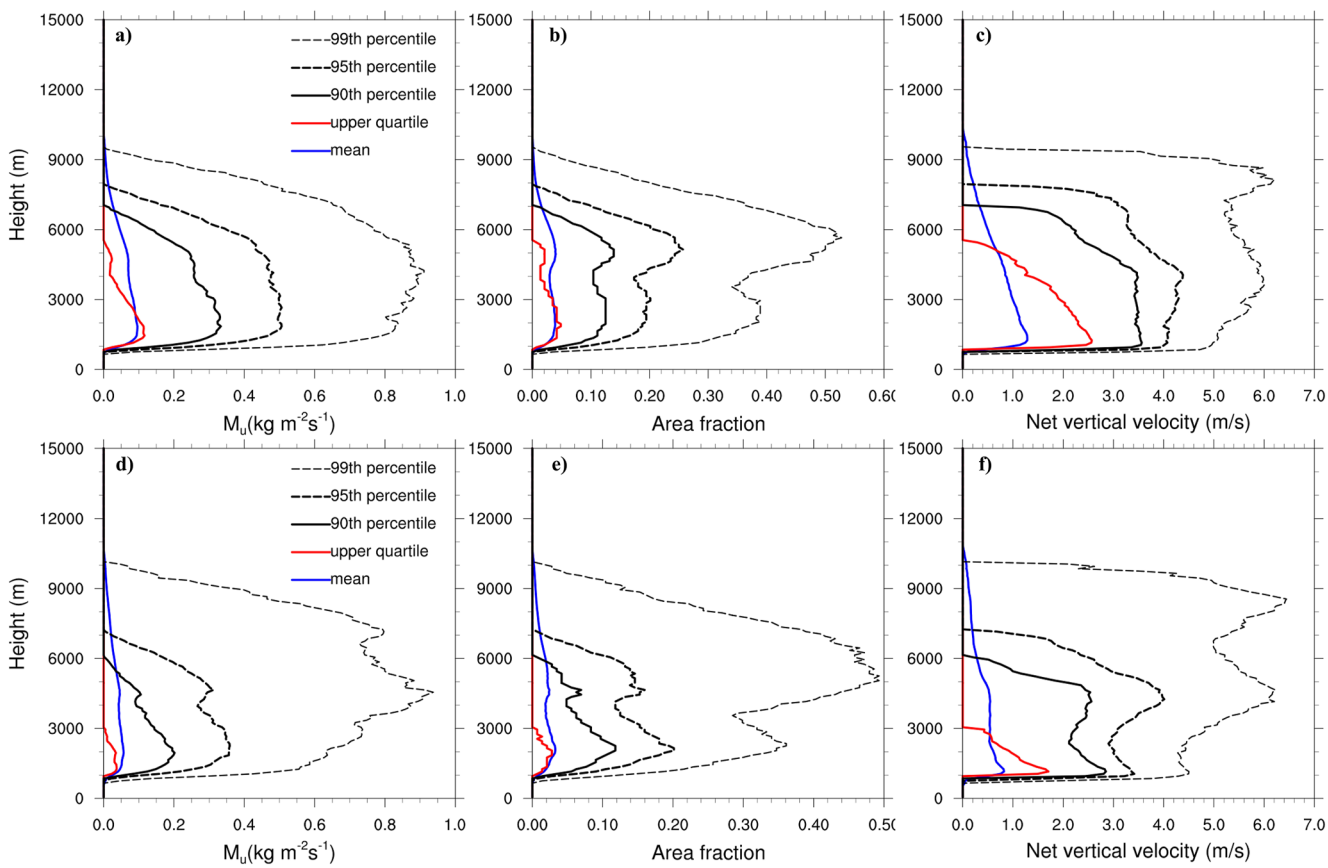

Figure 7. The ensemble mean (blue line), upper quartile (red line), 90th percentile (black line), 95th percentile (thick dashed black line), and 99th percentile (thin dashed black line) of the (a and d) updraft mass flux M_u, (b and e) area fraction a_u, and (c and f) net vertical velocity $w_u - \overline{w}$ for the (a–c) rapid intensification and (d–f) mature stage.

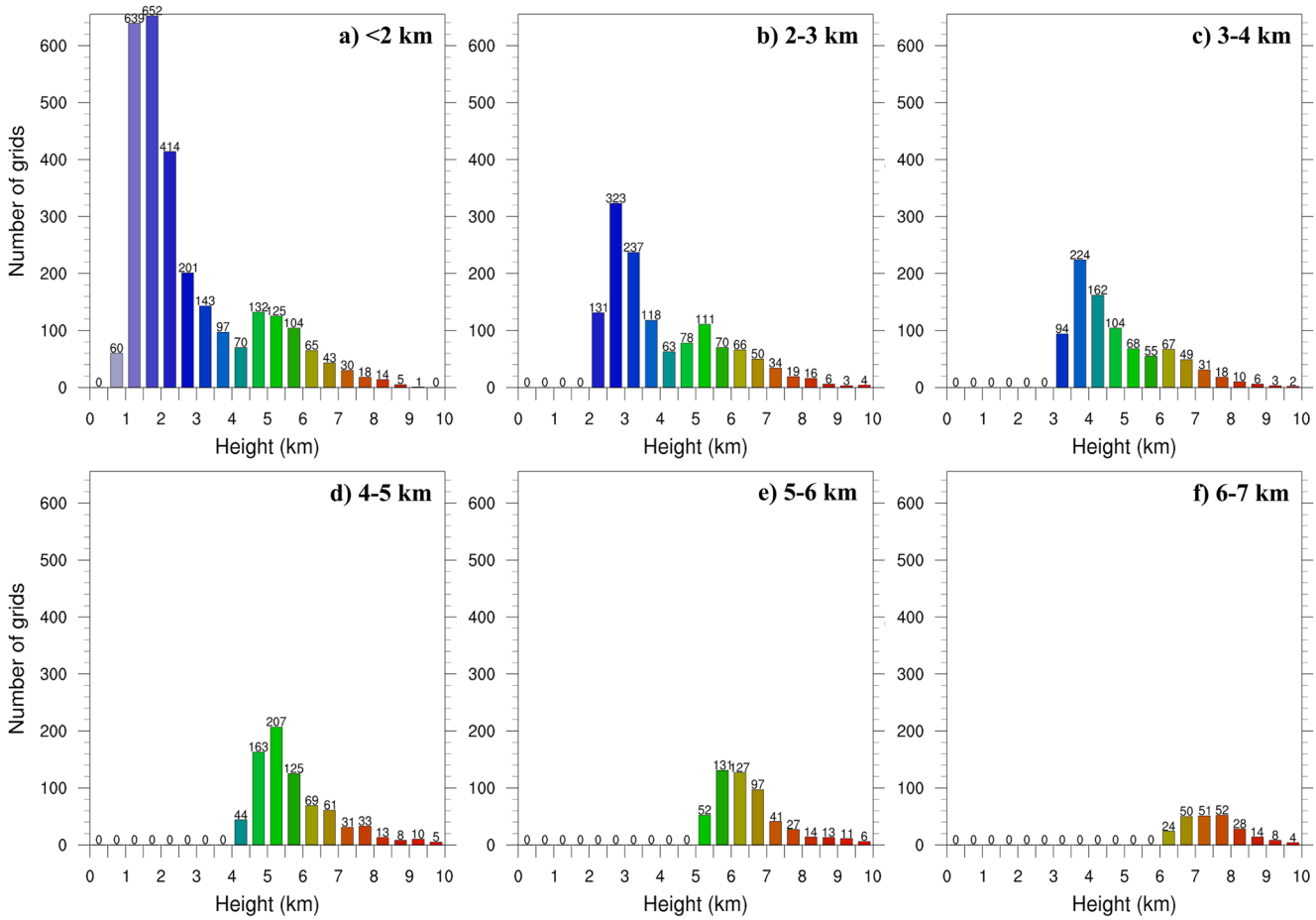

Figure 8. Histograms of cloud top height for various maximum mass flux height categories during the rapid intensification stage.

4.4. Composite Analysis by Maximum Mass Flux Height

We took advantage of the mass flux information in the coarse-grained LES data to separate all convective columns into categories according to the maximum mass flux height (MFH_{max}). For example, if the maximum mass flux height was located below 2 km, the corresponding columns were classified into the $MFH_{max} < 2$ km category. In this way, all convective columns were classified into seven categories, as follows: $MFH_{max} < 2$ km; 2 km $\leq MFH_{max} < 3$ km; 3 km $\leq MFH_{max} < 4$ km; 4 km $\leq MFH_{max} < 5$ km; 5 km $\leq MFH_{max} < 6$ km; 6 km $\leq MFH_{max} < 7$ km; and $MFH_{max} \geq 7$ km.

Figure 8 shows the CTH distributions for the various maximum MFH categories during the RI stage. The categories occupied 42%, 20%, 13%, 11.5%, 7.8%, 3.4%, and 1.7% of all convective columns, respectively. The number of convective columns decreased with MFH_{max}, indicating that the subgrid clouds were located primarily in the lower troposphere. The CTH of all categories was mainly located near the MFH_{max}. The small peaks between 5 and 7 km in Figures 8a–8c correspond to the peak at 5 km in Figure 6a. They mainly represent the subgrid clouds with two layers, the upper one of which is located between 5 and 7 km. Similar CTH distributions for the mature stage are shown in Figure 9, with the categories occupying 46.6%, 19.3%, 14%, 11.6%, 4.6%, 1.9%, and 1.8% of all convective columns, respectively. The difference from the RI stage is that there were no evident peaks between 5 and 7 km. These distributions reveal that the subgrid clouds were mainly located in the lower troposphere in both the RI and mature stage.

Having separated all the convective columns into maximum MFH categories, we then plotted the normalized composite vertical profiles of updraft mass flux for each category (Figure 10). There was a very clear separation in mass-flux shape and magnitude between categories (Figures 10a and 10b). The dark green line indicates an ensemble mean over all convective columns, which presents a well-known profile of mass flux with the average

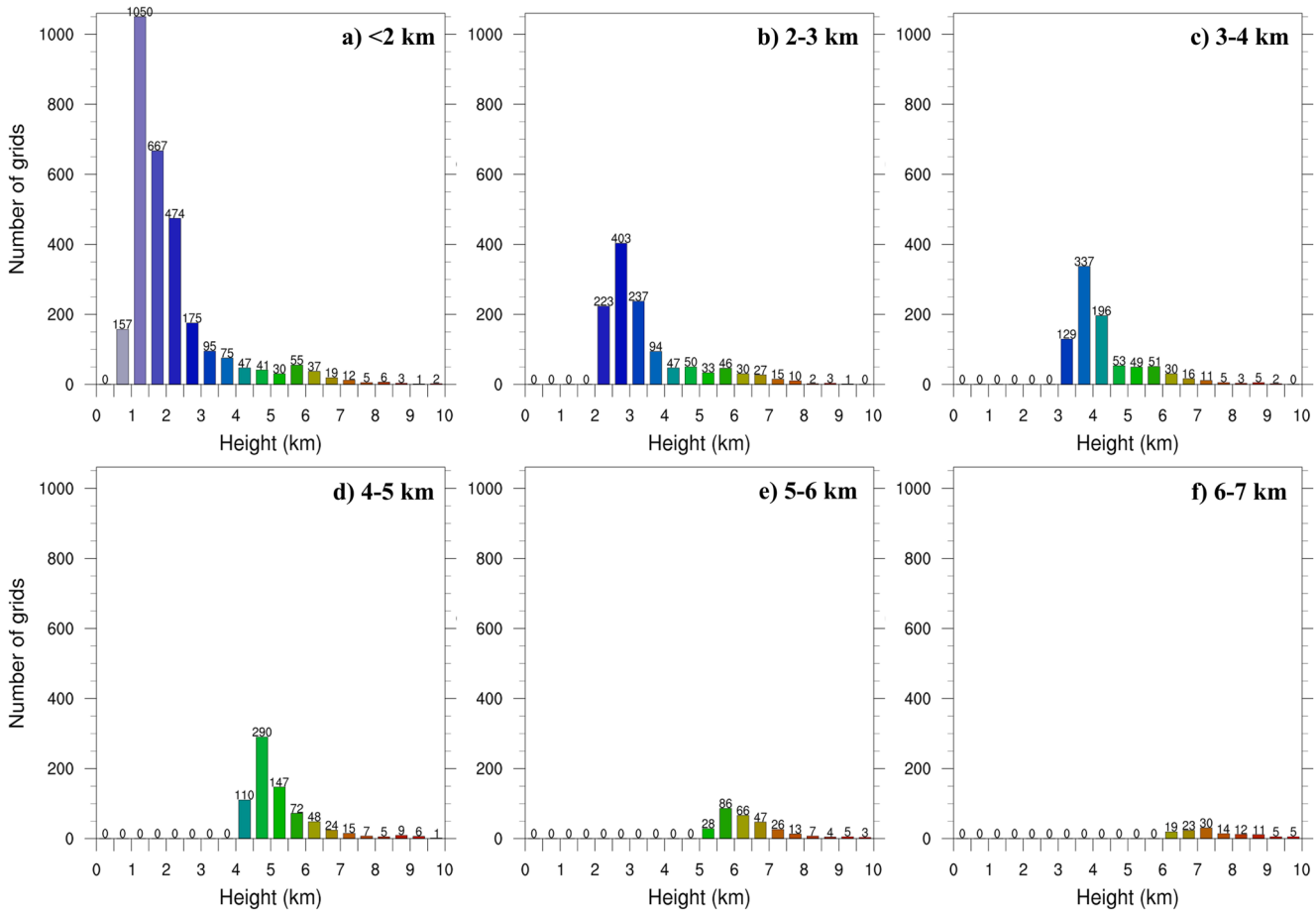

Figure 9. As in Figure 8 but for the mature stage.

property of the cloud ensemble. The classification identifies various cloud regimes under various parts of the TC system according to the maximum MFH. Each cloud regime had a vertical structure of mass flux distinct from that of the ensemble mean. The results imply that the ensemble mean shown in Figure 10 (dark green lines) is not needed in convection-permitting models. The local subgrid clouds that differ in magnitude and mass-flux profile shape at various locations in a convection system need to be represented in convection-permitting models.

It is worth noting that, to illustrate the relative contribution of each cloud regime to the ensemble-mean mass flux, the sum of updraft mass fluxes for each maximum MFH category was divided by the number of total convective column samples (not the respective number of convective column samples for each category) in Figures 10a and 10b. Hence, the values of updraft mass flux in Figures 10a and 10b were not absolute magnitudes, but including the information about the occurrence frequency of different cloud regime. The subgrid clouds with maximum MFH below 2 km occurred most frequently over the domain. The subgrid clouds with higher maximum MFH were much less frequent than the subgrid clouds with lower maximum MFH. Absolute magnitudes of updraft mass flux for various categories were shown in Figure S1.

The magnitude of M_u in the RI stage is larger than that in the mature stage (Figures 10a and 10b). Abundant convective towers are present during the RI stage. They are then organized into the eyewall and rainbands in the mature stage, while these organized convection systems are mostly resolved by model dynamics.

To further illustrate the subgrid convective effect, the subgrid vertical flux of the conserved variable moist static energy ($h = c_pT + Lq_v + gz$) was composited for each maximum MFH category, where c_p is the specific heat at constant pressure; T and q_v are the temperature and water vapor mixing ratio, respectively; L is the latent heat of vaporization; and gz is geopotential energy. For each category, the profile of $\overline{w'h'}$ presented similar vertical structures to the corresponding profile of mass flux (Figures 10c and 10d).

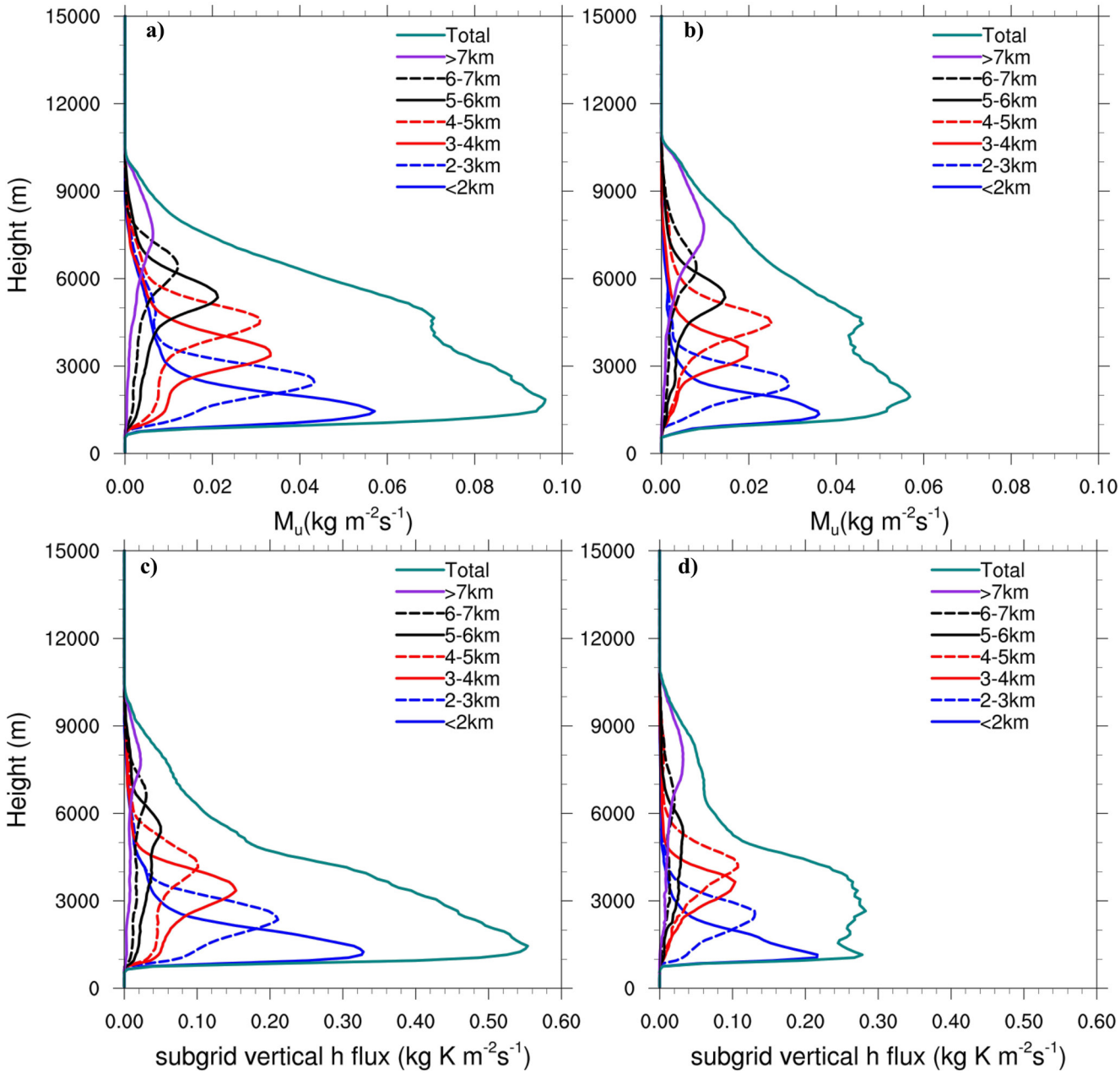

Figure 10. Normalized composite vertical profiles of (a and b) updraft mass flux M_u and (c and d) subgrid vertical moist static energy flux (divided by c_p) for various maximum MFH categories during the (a and c) rapid intensification and (b and d) mature stage. The dark green lines indicate ensemble mean over all convective columns. Note that the sum of fluxes for each maximum MFH category is divided by the number of total convective column samples (not the respective number of convective column samples for each category).

Figure 11 shows the spatial distributions of each maximum MFH category for the RI and mature stages. Different categories of subgrid clouds were scattered over the rainband in the RI stage (Figure 11a). The clouds in the mature stage showed more organized distributions than those in the RI stage (Figure 11b). Various subgrid clouds were distributed in a more orderly pattern over the portions of the rainband in the mature stage.

To build the closure relation between the subgrid cloud and grid-scale variables, the composite profiles of grid-scale vertical velocity $\overline{w}$ for each maximum MFH category are shown in Figure 12. The peak grid-scale vertical velocity corresponds to the maximum MFH for each category (Figures 10a and 12a). This indicates a good correlation between the subgrid cloud and grid-scale vertical motions, which provides a clue to the parameterized closure.

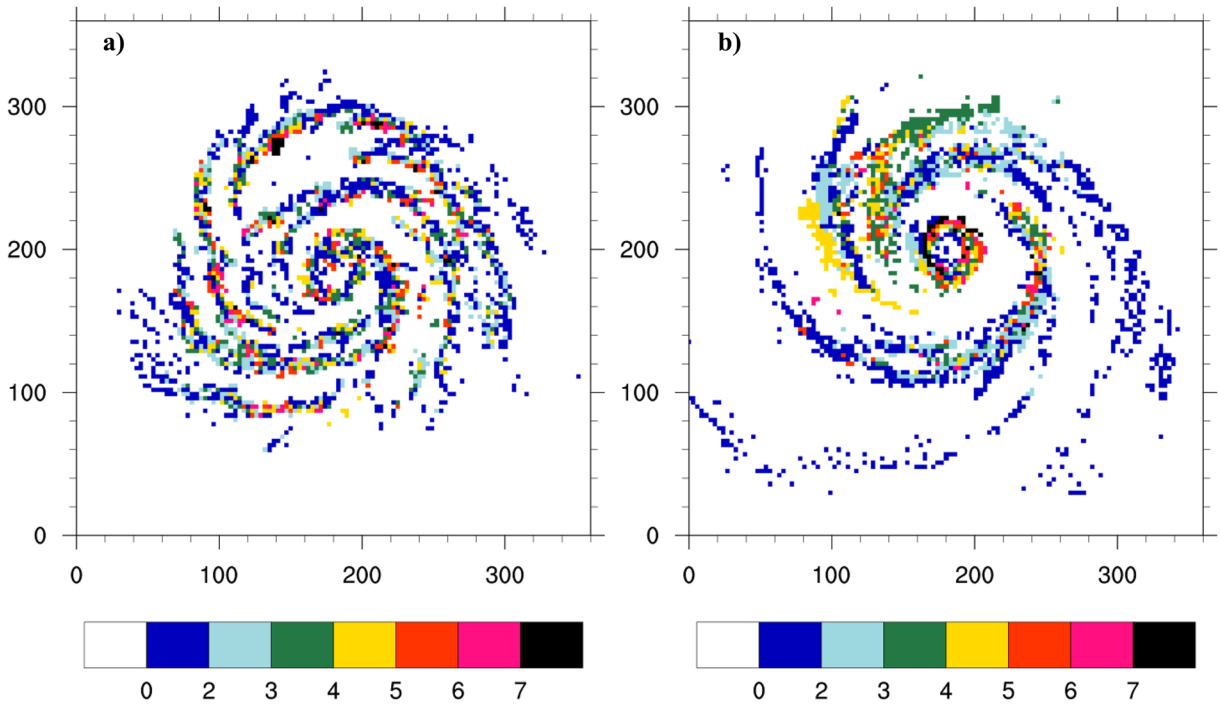

Figure 11. Spatial distributions of each maximum mass flux height category (indicated by the different colors) in the (a) rapid intensification and (b) mature stage. The blue color indicates the maximum MFH located between 0 and 2 km, and so on. The coordinates are in km.

Higher maximum MFH is associated with more intense convective cloud cores (Figures 12a and 12b), which is less frequent than shallow convective clouds with lower maximum MFH and weak $\overline{w}$ that are more widely spread over the domain (Figures 10 and 11). The higher the maximum MFH, the stronger the composite cloud updraft mass flux (See Figure S1). Although the absolute mass flux of shallow convective clouds with maximum MFH below 2 km is small (See Figure S1), they occur most frequently over the domain. Some studies showed that the shallow cumulus convection plays an important role in TC formation (Wang, 2014) and intensification (Kilroy, 2021). Due to the high frequency of occurrence, the parameterization for shallow convective clouds should be paid more attentions.

The composite profiles of grid-scale moist static energy show that the peak grid-scale upward motion ($\overline{w} > 0$) corresponded to local convective instability ($\partial h/\partial z < 0$) in the RI stage (Figures 12a and 12c). However, such correspondence between grid-scale $\overline{w}$ and local convective instability was not found for $\mathrm{MFH}_{\mathrm{max}} > 4$ km categories in the mature stage (Figures 12b and 12d), which indicates that the high-level subgrid clouds were not accounted for by the local buoyancy. For $\mathrm{MFH}_{\mathrm{max}} \leq 4$ km categories, there was a good correspondence among the grid-scale $\overline{w}$, subgrid cloud and local convective instability in both the RI and mature stage, which indicated that the low-level subgrid clouds were attributable to the local convective instability.

5. Summary and Discussion

LESs of an idealized TC were conducted as benchmarks to provide statistical information about the subgrid clouds at convection-permitting resolution over a TC convection system in different stages. Particular attention was given to the vertical and spatial distributions of the subgrid cloud and associated flux, which need to be parameterized in convection-permitting models. Results showed that the characteristics of the subgrid clouds varied significantly in various parts of the TC convection system. The statistics revealed that the subgrid clouds were mainly located in the lower troposphere and exhibited shallow vertical extents of less than 4 km. To examine the local subgrid-scale mass flux, the subgrid clouds were classified into various cloud regimes according to the maximum MFH. Composite analysis showed that local subgrid clouds differed in mass-flux profile shape and magnitude at various regimes in the TC convection system. The subgrid clouds with maximum MFH below 2 km occurred most frequently over the domain. A qualitative correlation between the grid-scale vertical velocity and

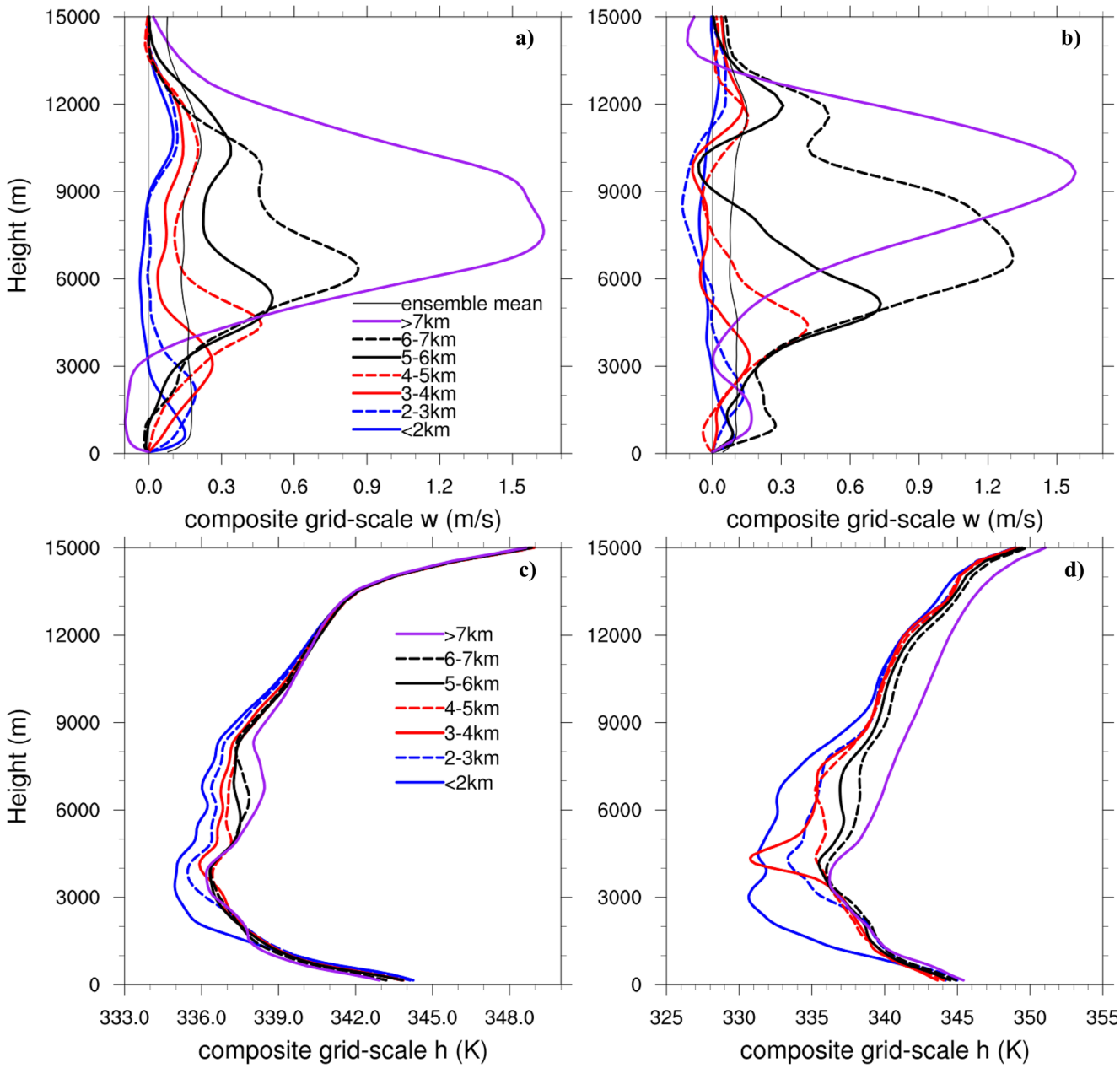

Figure 12. Composite profiles of grid-scale variables for various maximum MFH categories during the (a and c) rapid intensification and (b and d) mature stage. The thin gray line indicates the ensemble mean over all convective columns. For better illustration, the magnitude of the purple line in (b) for $MFH_{max} \geq 7$ km category is scaled by 1/3.

the subgrid clouds at various maximum MFH categories was shown, which suggests the use of the relationship for future developments of convection parameterizations at convection-permitting resolution.

Traditional convection parameterizations only consider the average properties of the cloud ensemble. Yanai et al. (1973) estimated the bulk properties of convective cloud ensemble from diagnostic analysis of radiosonde arrays. Recently, Savazzi et al. (2021) investigated the distribution of cloud ensemble mass flux profiles in an area comparable to a 100 km grid box from radar reflectivities spanning 13 wet seasons. Although these observational studies did not provide information on individual clouds and associated mass flux, they established reliable benchmarks for cloud ensembles that needed to be parameterized in traditional convection parameterizations. This study found that the subgrid cloud and associated mass flux at convection-permitting resolution exhibit profiles distinct from those of the cloud ensemble. At present, miscellaneous practices at convection-permitting

scale (Arakawa et al., 2011; Bechtold et al., 2008; Grell & Freitas, 2014; Kwon & Hong, 2017; Zheng et al., 2016) point to the lack of a benchmark. The situation prompted us to establish benchmarks that can depict the statistical characteristics of subgrid clouds at convection-permitting resolutions to guide the development of parameterizations for convection-permitting models. This paper represents an attempt to characterize statistical information about subgrid clouds for the convection-permitting resolution. This study also highlights the importance of establishing benchmarks using observations and LESs to develop and evaluate convection parameterization schemes suitable for models at convection-permitting resolutions.

The local subgrid clouds that differ in mass-flux profile shape and magnitude at various locations in a convection system need to be represented in convection-permitting models. This puts forward greater requirements for parameterization. In conventional mass flux models, the properties of the cloud ensemble are estimated from idealized steady-state entraining/detraining plume models. Once the entrainment and detrainment are specified, the corresponding mass-flux profile can be determined by the plume model. However, lateral mixing (entrainment/detrainment) between cloud and the environment is inherently difficult to parameterize. Previous studies (e.g., Böing et al., 2012; de Rooy et al., 2013) have mainly focused on the ensemble effect of entrainment and detrainment. Plume models might not be applicable at convection-permitting resolutions, particularly for the subgrid clouds with higher maximum MFH (Figure 10). Moeng (2014) proposed a closure for the updraft-downdraft mass flux framework to represent the subgrid-scale vertical fluxes of heat, moisture and momentum in convection-permitting models over the entire deep convection layer. This closure relates subgrid-scale fluxes to the horizontal gradient of local grid-scale resolvable variables and requires no building of the entraining/detraining plume model.

This study is a tentative attempt at examining the statistical characteristics of subgrid clouds at convection-permitting resolutions based on benchmark LES of a TC. The shear conditions in a TC environment will not be typical of tropical convection in general. Future studies will include more LESs under various meteorological regimes to analyze the subgrid-scale properties of cloud and to validate the convection parameterizations.

Data Availability Statement

The Advanced Research version of the Weather Research and Forecasting Model (WRF) version 4.3.1 (National Center for Atmospheric Research, 2021) is available from https://dx.doi.org/10.5065/D6MK6B4K. The data were analyzed with the NCAR Command Language version 6.6.2 (National Center for Atmospheric Research, 2019) available via http://dx.doi.org/10.5065/D6WD3XH5. The LES dataset and scripts for analysis are publicly available at (Zhang et al., 2022) https://doi.org/10.5281/zenodo.7344752.

Acknowledgments
This work was supported by the National Key Research and Development Program of China (2021YFC3000803), the National Natural Science Foundation of China (Grant 41975133) and the Research Program from Science and Technology Committee of Shanghai (Grant 19dz1200100). The authors thank two anonymous reviewers for their constructive suggestions and comments.

References

Arakawa, A., Jung, J.-H., & Wu, C.-M. (2011). Toward unification of the multiscale modeling of the atmosphere. *Atmospheric Chemistry and Physics*, *11*(8), 3731–3742. https://doi.org/10.5194/acp-11-3731-2011

Bao, J.-W., Gopalakrishnan, S. G., Michelson, S. A., Marks, F. D., & Montgomery, M. T. (2012). Impacts of physics representations in the HWRFX model on simulated hurricane structure and wind-pressure relationships. *Monthly Weather Review*, *140*(10), 3278–3299. https://doi.org/10.1175/mwr-d-11-00332.1

Bechtold, P., Koehler, M., Jung, T., Doblas-Reyes, F., Leutbecher, M., Rodwell, M. J., et al. (2008). Advances in simulating atmospheric variability with the ECMWF model: From synoptic to decadal time-scales. *Applied Meteorology, and Oceanography*, *134*(634), 1337–1351. https://doi.org/10.1002/qj.289

Bell, M. M., & Montgomery, M. T. (2010). Sheared deep vortical convection in pre-depression Hagupit during TCS08. *Geophysical Research Letters*, *37*(6), L06802. https://doi.org/10.1029/2009gl042313

Böing, S. J., Siebesma, A. P., Korpershoek, J. D., & Jonker, H. J. J. (2012). Detrainment in deep convection. *Geophysical Research Letters*, *39*(20), L20816. https://doi.org/10.1029/2012gl053735

Bryan, G. H., Wyngaard, J. C., & Fritsch, J. M. (2003). Resolution requirements for the simulation of deep moist convection. *Monthly Weather Review*, *131*(10), 2394–2416. https://doi.org/10.1175/1520-0493(2003)131<2394:rrftso>2.0.co;2

Deardorff, J. W. (1980). Stratocumulus-capped mixed layers derived from a three-dimensional model. *Boundary-Layer Meteorology*, *18*(4), 495–527. https://doi.org/10.1007/bf00119502

de Rooy, W. C., Bechtold, P., Froehlich, K., Hohenegger, C., Jonker, H., Mironov, D., et al. (2013). Entrainment and detrainment in cumulus convection: An overview. *Quarterly Journal of the Royal Meteorological Society*, *139*(670), 1–19. https://doi.org/10.1002/qj.1959

Donelan, M. A., Haus, B. K., Reul, N., Plant, W. J., Stiassnie, M., Graber, H. C., et al. (2004). On the limiting aerodynamic roughness of the ocean in very strong winds. *Geophysical Research Letters*, *31*(18), L18306. https://doi.org/10.1029/2004gl019460

Green, B. W., & Zhang, F. (2015). Numerical simulations of Hurricane Katrina (2005) in the turbulent gray zone. *Journal of Advances in Modeling Earth Systems*, *7*(1), 142–161. https://doi.org/10.1002/2014ms000399

Grell, G. A., & Freitas, S. R. (2014). A scale and aerosol aware stochastic convective parameterization for weather and air quality modeling. *Atmospheric Chemistry and Physics*, *14*(10), 5233–5250. https://doi.org/10.5194/acp-14-5233-2014

Han, J., Wang, W., Kwon, Y. C., Hong, S., Tallapragada, V., & Yang, F. (2017). Updates to the NCEP GFS cumulus convection schemes with scale and aerosol awareness. *Weather and Forecasting*, *32*(5), 2005–2017. https://doi.org/10.1175/waf-d-17-0046.1

Hong, S. Y., Noh, Y., & Dudhia, J. (2006). A new vertical diffusion package with an explicit treatment of entrainment processes. *Monthly Weather Review*, *134*(9), 2318–2341. https://doi.org/10.1175/mwr3199.1

Honnert, R., Masson, V., & Couvreux, F. (2011). A diagnostic for evaluating the representation of turbulence in atmospheric models at the kilometric scale. *Journal of the Atmospheric Sciences*, *68*(12), 3112–3131. https://doi.org/10.1175/jas-d-11-061.1

Houze, R. A., Jr. (2010). Clouds in tropical cyclones. *Monthly Weather Review*, *138*(2), 293–344. https://doi.org/10.1175/2009mwr2989.1

Houze, R. A., Jr., Lee, W.-C., & Bell, M. M. (2009). Convective contribution to the genesis of Hurricane Ophelia, 2005. *Monthly Weather Review*, *137*(9), 2778–2800. https://doi.org/10.1175/2009mwr2727.1

Jordan, C. L. (1958). Mean soundings for the West Indies area. *Journal of Meteorology*, *15*(1), 91–97. https://doi.org/10.1175/1520-0469(1958)015<0091:msftwi>2.0.co;2

Khairoutdinov, M. F., Krueger, S. K., Moeng, C.-H., Bogenschutz, P. A., & Randall, D. A. (2009). Large-eddy simulation of maritime deep tropical convection. *Journal of Advances in Modeling Earth Systems*, *1*(4), 15. https://doi.org/10.3894/james.2009.1.15

Kilroy, G. (2021). Evolution of convective characteristics during tropical cyclogenesis. *Quarterly Journal of the Royal Meteorological Society*, *147*(737), 2103–2123. https://doi.org/10.1002/qj.4011

Kwon, Y. C., & Hong, S.-Y. (2017). A mass-flux cumulus parameterization scheme across gray-zone resolutions. *Monthly Weather Review*, *145*(2), 583–598. https://doi.org/10.1175/mwr-d-16-0034.1

Lorsolo, S., Schroeder, J. L., Dodge, P., & Marks, F. (2008). An observational study of hurricane boundary layer small-scale coherent structures. *Monthly Weather Review*, *136*(8), 2871–2893. https://doi.org/10.1175/2008mwr2273.1

Marks, F. D., Black, P. G., Montgomery, M. T., & Burpee, R. W. (2008). Structure of the eye and eyewall of Hurricane Hugo (1989). *Monthly Weather Review*, *136*(4), 1237–1259. https://doi.org/10.1175/2007mwr2073.1

Moeng, C.-H. (2014). A closure for updraft-downdraft representation of subgrid-scale fluxes in cloud-resolving models. *Monthly Weather Review*, *142*(2), 703–715. https://doi.org/10.1175/mwr-d-13-00166.1

Moeng, C.-H., & Arakawa, A. (2012). Representation of boundary layer moisture transport in cloud-resolving models. *Monthly Weather Review*, *140*(11), 1520–0493. https://doi.org/10.1175/mwr-d-12-00046.1

Moeng, C.-H., Sullivan, P. P., Khairoutdinov, M. F., & Randall, D. A. (2010). A mixed scheme for subgrid-scale fluxes in cloud-resolving models. *Journal of the Atmospheric Sciences*, *67*(11), 3692–3705. https://doi.org/10.1175/2010jas3565.1

Montgomery, M. T., & Smith, R. K. (2014). Paradigms for tropical cyclone intensification. *Australian Meteorological and Oceanographic Journal*, *64*(1), 37–66. https://doi.org/10.22499/2.6401.005

Morrison, I., Businger, S., Marks, F., Dodge, P., & Businger, J. A. (2005). An observational case for the prevalence of roll vortices in the hurricane boundary layer. *Journal of the Atmospheric Sciences*, *62*(8), 2662–2673. https://doi.org/10.1175/jas3508.1

National Center for Atmospheric Research. (2019). The NCAR Command Language (Version 6.6.2) [Software]. UCAR/NCAR/CISL/TDD. https://doi.org/10.5065/D6WD3XH5

National Center for Atmospheric Research. (2021). Weather Research and Forecasting (WRF) model (Version 4.3.1) [Software]. NCAR. https://doi.org/10.5065/D6MK6B4K

Nguyen, V. S., Smith, R. K., & Montgomery, M. T. (2008). Tropical-cyclone intensification and predictability in three dimensions. *Quarterly Journal of the Royal Meteorological Society*, *134*(632), 563–582. https://doi.org/10.1002/qj.235

Ren, H., Dudhia, J., & Li, H. (2020). Large-eddy simulation of idealized hurricanes at different sea surface temperatures. *Journal of Advances in Modeling Earth Systems*, *12*(9), e2020MS002057. https://doi.org/10.1029/2020MS002057

Rotunno, R., Chen, Y., Wang, W., Davis, C., Dudhia, J., & Holland, G. J. (2009). Large-eddy simulation of an idealized tropical cyclone. *Bulletin of the American Meteorological Society*, *90*(12), 1783–1788. https://doi.org/10.1175/2009bams2884.1

Rotunno, R., & Emanuel, K. A. (1987). An air-sea interaction theory for tropical cyclones. Part II: Evolutionary study using a nonhydrostatic axisymmetric numerical model. *Journal of the Atmospheric Sciences*, *44*(3), 542–561. https://doi.org/10.1175/1520-0469(1987)044<0542:aaitft>2.0.co;2

Savazzi, A. C. M., Jakob, C., & Siebesma, A. P. (2021). Convective mass-flux from long term radar reflectivities over Darwin, Australia. *Journal of Geophysical Research: Atmospheres*, *126*(19), e2021JD034910. https://doi.org/10.1029/2021jd034910

Shi, X., Chow, F. K., Street, R. L., & Bryan, G. H. (2019). Key elements of turbulence closures for simulating deep convection at kilometer-scale resolution. *Journal of Advances in Modeling Earth Systems*, *11*(3), 818–838. https://doi.org/10.1029/2018ms001446

Siebesma, A. P., & Cuijpers, J. W. M. (1995). Evaluation of parametric assumptions for shallow cumulus convection. *Journal of the Atmospheric Sciences*, *52*(6), 650–666. https://doi.org/10.1175/1520-0469(1995)052<0650:eopafs>2.0.co;2

Skamarock, W. C., Klemp, J. B., Dudhia, J., Gill, D. O., Barker, D. M., Duda, M. G., et al. (2019). A description of the advanced research WRF Version 4 (NCAR Technical Note NCAR/TN-556+STR) (p. 145).

Smagorinsky, J. (1963). General circulation experiments with the primitive equations: I. The basic experiment. *Monthly Weather Review*, *91*(3), 99–164. https://doi.org/10.1175/1520-0493(1963)091<0099:Gcewtp>2.3.Co;2

Thompson, G., Field, P. R., Rasmussen, R. M., & Hall, W. D. (2008). Explicit forecasts of winter precipitation using an improved bulk microphysics scheme. Part II: Implementation of a new snow parameterization. *Monthly Weather Review*, *136*(12), 5095–5115. https://doi.org/10.1175/2008mwr2387.1

Wang, Z. (2014). Role of cumulus congestus in tropical cyclone formation in a high-resolution numerical model simulation. *Journal of the Atmospheric Sciences*, *71*(5), 1681–1700. https://doi.org/10.1175/jas-d-13-0257.1

Wu, L., Liu, Q., & Li, Y. (2018). Prevalence of tornado-scale vortices in the tropical cyclone eyewall. *Proceedings of the National Academy of Sciences*, *115*(33), 8307–8310. https://doi.org/10.1073/pnas.1807217115

Wurman, J., & Kosiba, K. (2018). The role of small-scale vortices in enhancing surface winds and damage in Hurricane Harvey (2017). *Monthly Weather Review*, *146*(3), 713–722. https://doi.org/10.1175/mwr-d-17-0327.1

Wurman, J., & Winslow, J. (1998). Intense sub-kilometer-scale boundary layer rolls observed in Hurricane Fran. *Science*, *280*(5363), 555–557. https://doi.org/10.1126/science.280.5363.555

Yanai, M., Esbensen, S., & Chu, J. H. (1973). Determination of bulk properties of tropical cloud clusters from large-scale heat and moisture budgets. *Journal of the Atmospheric Sciences*, *30*(4), 611–627. https://doi.org/10.1175/1520-0469(1973)030<0611:dobpot>2.0.co;2

Zhang, X., Bao, J. W., Chen, B., & Grell, E. D. (2018). A three-dimensional scale-adaptive turbulent kinetic energy scheme in the WRF-ARW model. *Monthly Weather Review*, *146*(7), 2023–2045. https://doi.org/10.1175/mwr-d-17-0356.1

Zhang, X., Bao, J. W., Huang, W., & Yu, H. (2022). Statistics of the subgrid cloud of an idealized tropical cyclone at convection-permitting resolution [Dataset]. Zenodo. https://doi.org/10.5281/zenodo.7344752

Zheng, Y., Alapaty, K., Herwehe, J. A., Del Genio, A. D., & Niyogi, D. J. M. W. R. (2016). Improving high-resolution weather forecasts using the Weather Research and Forecasting (WRF) Model with an updated Kain–Fritsch scheme. *Monthly Weather Review*, *144*(3), 833–860. https://doi.org/10.1175/mwr-d-15-0005.1

Zhu, P. (2008). Simulation and parameterization of the turbulent transport in the hurricane boundary layer by large eddies. *Journal of Geophysical Research*, *113*(D17), D17104. https://doi.org/10.1029/2007jd009643

Zhu, P., Tyner, B., Zhang, J. A., Aligo, E., Gopalakrishnan, S., Marks, F. D., et al. (2019). Role of eyewall and rainband in-cloud turbulent mixing in tropical cyclone intensification. *Atmospheric Chemistry and Physics*, *19*(22), 14289–14310. https://doi.org/10.5194/acp-19-14289-2019